





Highly Reliable Transmission System for Next-Generation Optical Access Network Based on Silicon Modulator With Maximum-Ratio Combined Receiver

Jun Qin, Yuansheng Tao, Haowen Shu , Siming Liu, Danshi Wang , Rahul Kumar Gangwar, Guo-Wei Lu , *Member, IEEE*, and Xingjun Wang 

Abstract—A novel maximum-ratio combined receiver (MRC-RX) is proposed and demonstrated through a proof-of-concept experiment, conducted to mitigate the system performance degradation caused by the low linearity of the silicon modulator when deployed in passive optical network (PON)-based access. By employing the proposed MRC-RX, an optimized receiver sensitivity is achieved, which enables the mitigation of the performance degradation induced by the silicon modulator, and a more reliable transmission in both cases of low and high received power. In the proof-of-concept experiment, at a bit error rate of 1.0×10^{-4} , the receiver sensitivity of the MRC-RX was improved by 3.5 dB and 6.7 dB compared with the lite coherent receiver (lite CO-RX) and direct detection receiver (DD-RX), respectively. Compared with a system employing a commercial lithium niobate (LiNbO₃) modulator, a maximum improvement of ~ 5.6 dB in the receiver sensitivity was obtained for the MRC-RX in the silicon modulator system. Thus, the system performance degradation caused by the low linearity of the silicon modulator can be effectively reduced by employing the MRC-RX. The proposed method makes sense to the building of next generation high reliable photonics integrated access by employing silicon modulators.

Index Terms—Lite-coherent, modulator linearity, passive optical network, silicon modulator.

I. INTRODUCTION

PRESENTLY, the development of new 5G-enabled, ultra-reliable low latency communications (uRLLC) services, such as remote industrial control, automated driving, and remote surgery/e-health, has increased the demands for the network reliability of optical access network [1]–[3]. The passive optical network (PON) with a tree topology has been regarded as the most attractive optical access network architecture [4], [5]. The standardization of next-generation optical access networks, such as wavelength-division multiplexing (WDM) PONs [2], [5], and next-generation passive optical network stage 2 (NG-PON2) is being actively advanced [6]. As a promising next-generation PON candidate for optical access network, NG-PON2 exploits time- and wavelength-division multiplexing (TWDM). Each optical line terminal (OLT) communicates with multiple optical network units (ONUs) via time-division multiple access, while different wavelengths are used between different OLTs. Moreover, NG-PON2 is expected to be compatible with the legacy optical distribution network (ODN) with power-splitter-based fiber infrastructure [6]. In ODN, with a high split ratio, the expense of per-ONU can be reduced as more sites can be supported by a single feeder fiber. To comply with the new standard, approaches using coherent detection have been proposed for PON-based access network [4], [7]. Compared to the currently employed direct-detection receivers (DD-RX), coherent detection receivers (CO-RX) offer significantly higher receiver sensitivities that can enable a higher split ratio and longer reach for PON. Moreover, CO-RX exhibits significant advantages, such as robustness to chromatic dispersion [8], colorless receiver operation due to its wavelength/frequency selectivity, and high achievable spectral-efficiency through the realization of high-order modulation formats. However, the conventional in-tradyne coherent receiver, which comprises components such as polarization-diversity hybrid and balanced-photodetector array, is extremely complicated and expensive for PON. To decrease the complexity and cost, lite coherent receivers (lite CO-RX) have been proposed and employed in the work of [4], [7].

Manuscript received February 21, 2020; revised August 8, 2020 and September 1, 2020; accepted September 1, 2020. Date of publication September 4, 2020; date of current version October 2, 2020. This work was supported in part by the Beijing Key R&D Project No. Z19110004819006, in part by National Natural Science Foundation of China under Grant 61635001, in part by National Key R&D Project No. 2018YFB2201704, and in part by China Postdoctoral Science Foundation under Grant 2019M660326 (*Corresponding author: Xingjun Wang.*)

Jun Qin, Yuansheng Tao, Haowen Shu, and Rahul Kumar Gangwar are with the State Key Laboratory of Advanced Optical Communication Systems and Networks, Department of Electronics, School of Electronics Engineering and Computer Science, Peking University, Beijing 100871, China (e-mail: qinjun5566_pek@126.com; ystao@pku.edu.cn; haowenshu@pku.edu.cn; rahul@pku.edu.cn).

Siming Liu and Danshi Wang are with the Beijing University of Posts and Telecommunications, Beijing 100876, China (e-mail: liu567c@163.com; danshi_wang@bupt.edu.cn).

Guo-Wei Lu is with the University of Aizu, Fukushima 965-8580, Japan (e-mail: gordon.guoweilu@gmail.com).

Xingjun Wang is with the State Key Laboratory of Advanced Optical Communication Systems and Networks, Department of Electronics, School of Electronics Engineering and Computer Science, Peking University, Beijing 100871, China, and also with the Nano-optoelectronics Frontier Center of Ministry of Education and Peking University Yangtze Delta Institute of Optoelectronics, Peking University, Beijing 100871, China (e-mail: xjwang@pku.edu.cn).

Color versions of one or more of the figures in this article are available online at <https://ieeexplore.ieee.org>.

Digital Object Identifier 10.1109/JSTQE.2020.3021732

Compared to the conventional intradyne coherent receiver, by employing heterodyne coherent detection combined with digital signal processing (DSP), the receiver complexity is substantially reduced (a single photodetector (PD) is required) in the lite coherent receiver, as reported in [4], [7]. The achieved high sensitivity and low cost of lite CO-RX makes it a promising receiver candidate for an access network. However, the performance of lite CO-RX is significantly influenced by the frequency offset and phase noise generated by the two beating laser sources, although many carrier phase recovery (CPR) and carrier frequency offset (CFO) algorithms have been proposed to solve this problem. In the case of a high received optical power, the recovered signal from CO-RX is still inferior to that from DD-RX [4], [9]. By separately employing DD-RX and lite CO-RX, the best receiver sensitivity cannot be simultaneously maintained for low and high received optical power, which is not conducive to build a highly reliable PON access to meet the transmission requirements for services such as uRLLC in the 5G era.

Silicon photonics is considered a promising technology to address the challenge of chip-scale integrated communication systems owing to the compactness for high-density integration and complementary metal-oxide semiconductor (CMOS) compatibility for low-cost mass production [10]. Fabricating optical devices into the silicon platform in the access network can reduce the size and weight of the access equipment, as well as reduce the power consumption and cost. Silicon photonics on silicon on insulator platform has emerged as the leading technology. Optical modulators are fundamental components of optical communication links and serve as the information encoding engines from the electrical domain to the optical domain [11]. The traditional lithium niobate (LiNbO_3) modulators are costly and difficult to be integrated; therefore, researchers are continuously attempting to discover a low-cost and easily integrated modulator device. A silicon-based modulator is a suitable candidate. Silicon traveling-wave Mach-Zehnder modulators (TW-MZM) utilizing carrier-depletion-type phase shifters have been widely integrated as fundamental devices [12]–[17]. Carrier depletion in a reverse-biased pn diode offers a high-speed response due to its small capacitance, but it is intrinsically absorptive and nonlinear, moreover, it suffers from low linearity, which will cause distortions to the generated signal [18]–[20]. Various efforts have been made to improve this, including the optimization of pn diode designs, doping density, novel waveguide structure, electrode designs, and driving methods [19], [21], [22]. All these methods require changing of the physical characteristics/structures or addition of extra electrical driving circuits; they are predetermined before fabrication or packaging, thus, can be regarded as prefabrication/packaging optimizations.

In this paper, a novel maximum-ratio combined receiver (MRC-RX) is proposed and demonstrated through a proof-of-concept experiment, conducted to mitigate the system performance degradation caused by the low linearity of the silicon modulator when deployed in PON-based access. By employing the proposed MRC-RX, an optimized receiver sensitivity was achieved that enables the mitigation of the performance degradation induced by the silicon modulator, and a more reliable

transmission in both cases of low and high received power. The proposed MRC-RX is an algorithm-based post-fabrication performance optimization method for a silicon modulator, which has not been reported before.

The paper is organized as follows. In section II, the working principle and experimental setup are introduced, the experiment results are presented in section III. The cost and the potential methods that can be used to further improve the system are discussed in section IV. Finally, the paper is concluded in Section V.

II. WORKING PRINCIPLE AND EXPERIMENTAL SETUP

Fig. 1 demonstrates the framework, working principle, and experimental setup of the access prototype based on a silicon modulator with the proposed MRC-RX. Different OLTs ($\#OLT1, \dots, \#OLTn-1, OLTn$) of different wavelengths are coupled together through WDM. After transmission via ODN, which comprises transmission fiber, WDM demultiplexer, and passive splitters/combiners, the signals arrive at ONU. Multiple ONUs ($ONU1, \dots, ONUn-1, ONUn$) communicate with the OLTs through an optical power splitter. In the figure, the downstream channels (OLT->ONU) and upstream channels (ONU->OLT) are indicated by red and purple lines, respectively.

The continuous-wave (CW) laser in OLT/ONU works simultaneously as the local oscillator (LO) laser for the upstream/downstream signal and the source laser for the downstream/upstream signal. By tuning the wavelength of the LO, arbitrary wavelength channel selection can be achieved. For the downstream situation, the optical spectra of the downstream signal at f_1 with two sidebands before (point 1) and after (point 2) adding the LO at f_2 in the ONU are shown in Insets (1) and (2). After the square law detection in a PD, the electrical frequency spectra of the received signal at point 5 is presented in Inset (5).

As shown in Inset (5), the DD-RX component at intermediated frequency f_{IF1} is generated by the beating between the downstream optical carrier and the downstream signal sidebands. As the DD-RX component is produced by the same laser, it is free of CFO and carrier phase noise. The lite CO-RX component at f_{IF2} , which satisfies $f_{IF2} = f_1 - f_2 - f_{IF1} = \Delta f - f_{IF1}$ (Δf is the frequency offset between the downstream laser and upstream laser which working as the LO in the downstream case), is generated from the beating between the LO light and the lower sideband of the downstream signal at $f_1 - f_{IF1}$. As the lite CO-RX component is produced by two laser sources, CFO and CPR algorithms are required to recover the signal.

After the separate DSPs for the DD-RX and lite CO-RX, a maximum-ratio combined (MRC) algorithm, represented by equation (1), was employed to calculate the output signal as the results of MRC-RX [23]–[25].

$$S_{MRC-RX}(t) = \frac{SNR_{DD-RX}}{SNR_{DD-RX} + SNR_{liteCO-RX}} S_{DD-RX}(t) + \frac{SNR_{liteCO-RX}}{SNR_{DD-RX} + SNR_{liteCO-RX}} S_{liteCO-RX}(t) \quad (1)$$

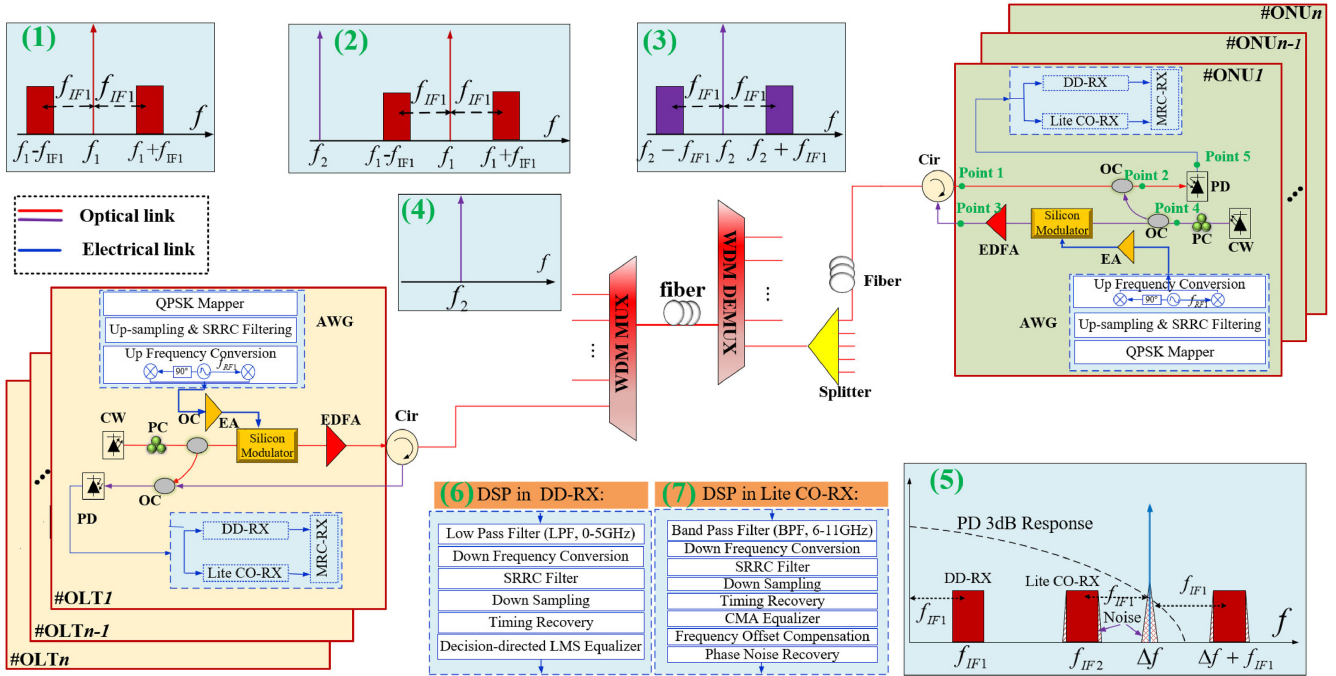


Fig. 1. Framework and experimental setup of the PON based access network prototype based on an MRC-RX using silicon modulator. Inset (1): optical spectrum of the downstream signal at f_1 with two sidebands at $f_1 + f_{RF1}$ and $f_1 - f_{RF1}$; Inset (2): optical spectrum of the downstream signal after adding LO at f_2 ; Inset (3): optical spectrum of the upstream signal at f_2 with two sidebands at $f_2 + f_{RF1}$ and $f_2 - f_{RF1}$; Inset (4): optical spectrum of the upstream light; Inset (5): electrical spectrum of the received signal after square law detection of PD; Inset (6): DSP in the DD-RX; Inset (7): DSP in the lite CO-RX. PON: passive optical network, MRC-RX: maximum-ratio combined receiver, LO: local oscillator, DD-RX: direct detection receiver, lite CO-RX: lite coherent receiver, OLT: optical line terminal, ONU: optical network unit, CW: continuous wave, PC: polarization controller, OC: optical coupler, AWG: arbitrary waveform generator, EA: electrical amplifier, EDFA: erbium-doped fiber amplifiers, Cir: circulator, WDM MUX/DEMUX: wavelength-division multiplexer/demultiplexer, PD: photodetector, DSP: digital signal processing, SRRC: square root raise cosine, DD-LMS: decision-directed least mean square equalizer, CMA: constant modulus algorithm, QPSK: quadrature phase shift keying.

In equation (1), $S_{MRC-RX}(t)$, $S_{DD-RX}(t)$, and $S_{lite\ CO-RX}(t)$ are the output signals from the MRC-RX, DD-RX, and lite CO-RX, respectively. SNR represents the signal-noise ratio of the different receivers, which can be calculated using the error vector magnitude (EVM). $SNR_{DD-RX}/(SNR_{DD-RX}+SNR_{lite\ CO-RX})$ and $SNR_{lite\ CO-RX}/(SNR_{DD-RX}+SNR_{lite\ CO-RX})$ represent the maximal SNR ratios achieved for the DD-RX and lite CO-RX, respectively. As the recovered signal quality from the DD-RX and lite CO-RX is directly determined by the SNR , it is reasonable to combine the results based on different SNR ratios in MRC-RX, as identified in [24]. For the upstream transmission, the signal and LO laser frequency can be replaced with f_2 and f_1 ; insets (3–4) show the corresponding optical spectra of the upstream light after and before use with the modulator.

The proof-of-concept experimental setup for downstream transmission with the proposed MRC-RX is also shown in Fig. 1. In the experiment, the downstream quadrature phase shift keying (QPSK) signal at $f_{IF1} = 2.5$ GHz is first generated by an arbitrary waveform generator (AWG, Tektronix 70002) in OLT. Square-root-raised-cosine (SRRC) filtering is used to convolve each transmitted symbol waveform truncated from $-8T$ to $8T$ (T is the symbol duration) with a roll-off factor of 0.1 after up-sampling. The data rate of the generated QPSK signal is 2.5 Gbps. The signals are converted to intermediate frequency analog waves by the AWG, which then drive the silicon modulator. A CW laser at the wavelength of 1,549.951 nm (Agilent N7714A) was

followed by a polarization controller (PC) before being injected into the silicon modulator. Afterward, an erbium-doped fiber amplifier (EDFA) was used to amplify the signal. After standard single-mode fiber (SSMF) transmission, the signal arrives at ONU. In the receiver, upstream CW light at the wavelength of 1,550.043 nm (Yokogawa AQ2200, with ~ 1.5 -MHz linewidth) is used as the LO to beat with the downstream signal light (the frequency interval between the signal light and LO $\Delta f = f_1 - f_2 = 11.5$ GHz) in the PD (with 12.5 GHz 3 dB bandwidth) to generate the lite CO-RX component. The PC behind the LO is employed to obtain the best heterodyne performance in the PD by adjusting the polarization states. The MRC-RX includes two parts: DD-RX and lite CO-RX. The two parts' results will be combined as the outputs of the MRC-RX through the MRC algorithm presented as equation (1).

The DSPs for the DD-RX and lite CO-RX are shown in Insets (6) and (7) in Fig. 1, respectively. For the DD-RX, a low-pass filter of 0–5 GHz was first utilized to filter the signal at f_{IF1} . After down-frequency conversion, a matching SRRC filter was employed to recover the original QPSK waveforms. Because the received signal is sampled at a fixed rate by the free-running oscilloscope and all further processing be done digitally using these samples, a clock recovery algorithm is necessary to estimate the timing offset between the real samples and the optimal sampling points. In this experiment, a square timing recovery algorithm was used for both the DD-RX and

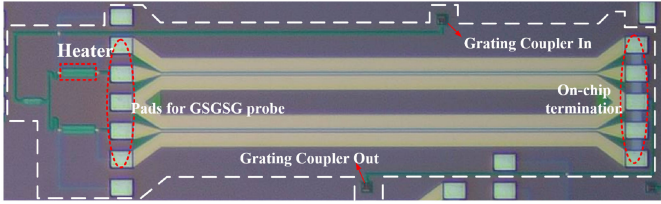


Fig. 2. Micrograph of the employed silicon traveling-wave Mach-Zehnder modulator.

lite CO-RX [26]. Finally, a decision-directed least mean square (DD-LMS) equalizer with 101 T symbol duration delay taps was employed to equalize the linear impairments. For the lite CO-RX, a bandpass filter (BPF) with a passband of 6–11 GHz was first used to select the lite CO-RX component. After BPF filtering, down-frequency conversion from f_{IF2} will be carried out. The subsequent SRRC filtering, down sampling, and clock recovery are the same as those in the DD-RX. However, instead of a DD-LMS equalizer, a constant modulus algorithm equalizer with 101 $T/2$ symbol duration delay taps was employed in the lite CO-RX. As the component of the lite CO-RX is susceptible to the phase-related impairments introduced by the two incoherent beating lasers, the DD-LMS is unable to converge. In the last two steps, CFO and CPR algorithms [27], [28] are used to compensate the frequency offset and phase related impairments. Finally, the results of the DD-RX and lite CO-RX are combined using the MRC algorithm shown in equation (1) as the outputs of the MRC-RX.

III. EXPERIMENTAL RESULTS AND ANALYSIS

A. Characterization of the Silicon Modulator

The silicon TW-MZM chip used in the experiment was fabricated by Interuniversity Microelectronics Centre (IMEC, Belgium), the structure is shown in Fig. 2. The modulator used in the experiment is highlighted by the white dashed line in the figure. On the left side of the signal lines, a group of GSGSG (G: Ground, S: Signal) pads were built to apply the bias voltage and the driving signal through the electrical radiofrequency (RF) probe (MPI T50A G5100). In the experiment, single-arm driving was employed, and the light was coupled in and out of the modulator by fiber-to-chip grating couplers with an intersection loss of ~ 6 dB/coupler. The insertion loss of the modulator was measured to be 3.3 dB. Furthermore, each arm of the modulator contains a 1.5-mm long phase shifter, which works via the plasma dispersion effect; the voltage-length $V_{\pi}L$ of each modulation arm is 2.494 V.cm. Each signal line is terminated with an on-chip resistor to match closely with the impedance of the transmission line. The waveguides of the two arms were intentionally designed to be 100 nm away from the modulation region, which allows adjustment of the operation point via wavelength tuning.

The measured bandwidth of the silicon modulator is shown in Fig. 3. From the results, we can see that, as the reverse bias voltage changed from 0 V to 4 V, the 3-dB bandwidth of the modulator gradually increased from 23 GHz to 33 GHz. The

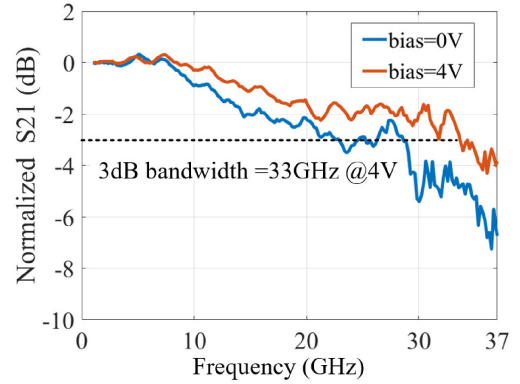


Fig. 3. Normalized electro-optic S21 response (bandwidth) of the silicon modulator at different reverse bias voltages.

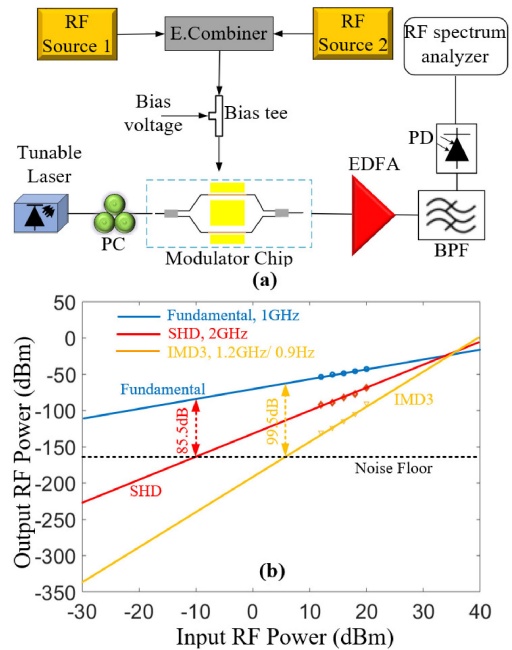


Fig. 4. (a) Experimental setup of the SFDR test; (b) RF output power of the fundamental, SHD, and IMD3 components as a function of the RF input power for our devices at 1 GHz and 1.1 GHz. SFDR: spurious free dynamic range, RF: radio frequency, E. Combiner: electrical combiner, EDFA: erbium-doped fiber amplifier, BPF: bandpass filter, PD: photodetector, PC: polarization controller, BPF: bandpass filter, SHD: second harmonic distortion, IMD3: third-order intermodulation.

variation of the bandwidth is mainly due to the change in the lateral pn junction capacitance caused by a different bias voltage. In the following experiments, 4 V was chosen as the reverse bias, corresponding to 33 GHz 3 dB bandwidth.

To characterize the linearity of the present modulator, the second harmonic distortion (SHD) and third-order intermodulation (IMD3) spurious free dynamic range (SFDR) performance are further examined. Fig. 4(a) shows the experimental setup for the SFDR test. The light beam from a tunable laser source was coupled into and out of the fabricated modulator by grating couplers, as introduced previously. A PC was used to adjust the polarization state of the light injected into the chip. An EDFA

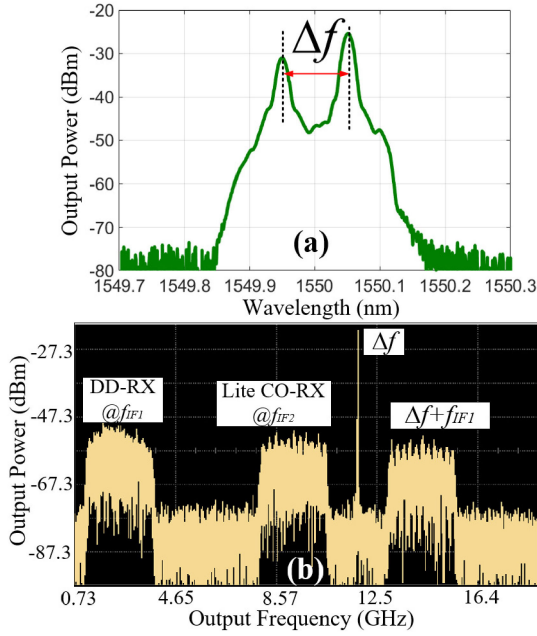


Fig. 5. (a) Optical spectra of the downstream signal light and upstream LO light; (b) Electrical spectrum captured from oscilloscope after PD. QPSK: quadrature phase shift keying, LO: local oscillator.

was employed to amplify the optical signal to meet the power requirement of the photodiode. Two microwave signals at two near frequencies $f_1 = 1$ GHz and $f_2 = 1.1$ GHz were first combined using an electrical combiner and then injected into a bias tee to drive the modulator. An electrical spectral analyzer after PD was used to measure the distortion components. Fig. 4(b) shows the measurement results, as the input power varies, the output powers of the fundamental signal at 1 GHz, SHD at 2 GHz, and IMD3 at 1.1 GHz/0.9 GHz (the IMD3 value shown in Fig. 4(b) is the mean value at 1.1 GHz and 0.9 Hz) can be recorded. In the figure, the points of SHD and IMD3 are fitted for calculation of the SFDRs according to a system noise floor of -161 dBm/Hz. For the employed modulator, the calculated SFDRs for SHD and IMD3 are 85.5 dB·Hz $^{1/2}$ and 99.5 dB·Hz $^{2/3}$, respectively.

B. Performance Measurements for DD-RX, Lite CO-RX, and MRC-RX

Fig. 5(a) shows the optical spectra of the received downstream QPSK signal and the upstream LO light before the PD. The electrical spectra after beating in the PD are presented in Fig. 5(b), captured using the oscilloscope (Keysight Infinium DSA 96204Q, running at 80 GSa/s, minimum sample rate requirement ~ 34.5 GSa/s) after fast Fourier transformation. From Fig. 5(b), we can see that the electrical signals detected by the DD-RX and lite CO-RX centered at $f_{IF1} = 2.5$ GHz and $f_{IF2} = 9$ GHz were successfully generated and obtained. The lite CO-RX frequency f_{IF2} is determined by the frequency intervals between the downstream signal, LO, and f_{IF1} , which satisfies $f_{IF2} = f_1 - f_2 - f_{IF1} = \Delta f - f_{IF1}$. Meanwhile, we can also obtain a component at frequency $\Delta f + f_{IF1} = 14$ GHz, but this is out of the 3-dB bandwidth of the PD and, thus, will be neglected.

Subsequently, the signals were captured by the oscilloscope and processed offline in MATLAB, as described in section II.

The bit error rate (BER) performance over the received power was calculated by comparing the difference between the original and recovered bits sequence in Fig. 6 for (a) back-to-back (BTB) and (b) 20-km SSMF transmission, respectively. An optical attenuator was used at the ONU side to change the received power. The results in Fig. 6(a) indicate that, by employing the MRC-RX at a BER of 1.0×10^{-4} , the receiver sensitivity was improved by 3.5 dB and 6.7 dB, as compared with the lite CO-RX and DD-RX, respectively. In Figs. 6(a) and (b), a similar BER variation tendency is achieved for different receivers for both BTB and 20-km SSMF transmission. For the 20-km SSMF transmission case, as shown in Fig. 6(b), when the received power is less than -17 dBm, the output signal quality of the MRC-RX is completely determined by the lite CO-RX because the DD-RX vanishes due to the low sensitivity of direct detection. However, when the power is larger than -17 dBm, because the MRC-RX combines the results of both the lite CO-RX and DD-RX, a better BER performance is achieved (1.92×10^{-5} at -7 dBm), as compared with the DD-RX (3.52×10^{-5}) and lite CO-RX (5.51×10^{-5}) individually. The demodulated constellation diagram shown in the right column is clearer and more concentrated for the MRC-RX than for the DD-RX and lite CO-RX. When the received power is larger than ~ -8 dBm, the DD-RX performs better than the lite CO-RX because it is immune to the phase-related impairments generated by the beating of different lasers. The receiver sensitivity of the lite CO-RX at 3.8×10^{-3} can be further improved by employing a narrow linewidth LO laser, which will be discussed in section IV.

C. Influences of Frequency Interval for Different Receivers

As the frequency interval between the DD-RX and lite CO-RX is determined by f_1 , f_2 , and f_{IF1} , careful calculation is necessary to avoid frequency overlap. Frequency overlap will cause severe performance degradation for different receivers. Fig. 7(a) illustrates the EVM performances with different frequency intervals (Δf) between f_1 and f_2 for the DD-RX, lite CO-RX, and MRC-RX after 20-km SSMF transmission, respectively. From the figure, we can see that, when $\Delta f < 10$ GHz, the EVM of the DD-RX, lite CO-RX, and MRC-RX all degrade, which is caused by the frequency overlap between the DD-RX and lite CO-RX.

Fig. 7(b) shows the captured electrical spectra when the received power is -6 dBm and the frequency interval is 10.5 GHz, from the demodulated signal constellation shown in (c)–(e), we can see that the signal quality of the lite CO-RX, DD-RX, and MRC-RX is maintained well. Compared to the lite CO-RX, $\sim 28.5\%$ EVM is enhanced for the MRC-RX. Meanwhile, when $\Delta f > 14$ GHz, the performance of the lite CO-RX starts to decrease because the signal is out of the 3-dB bandwidth of the PD. A higher bandwidth PD can support a larger frequency interval. Meanwhile, the DD-RX is not influenced and its performance remains at a suitable level. For the MRC-RX, the changing tendency is similar to the lite CO-RX. The results indicate that the optimal frequency interval between f_1 and f_2 is 10–14 GHz.

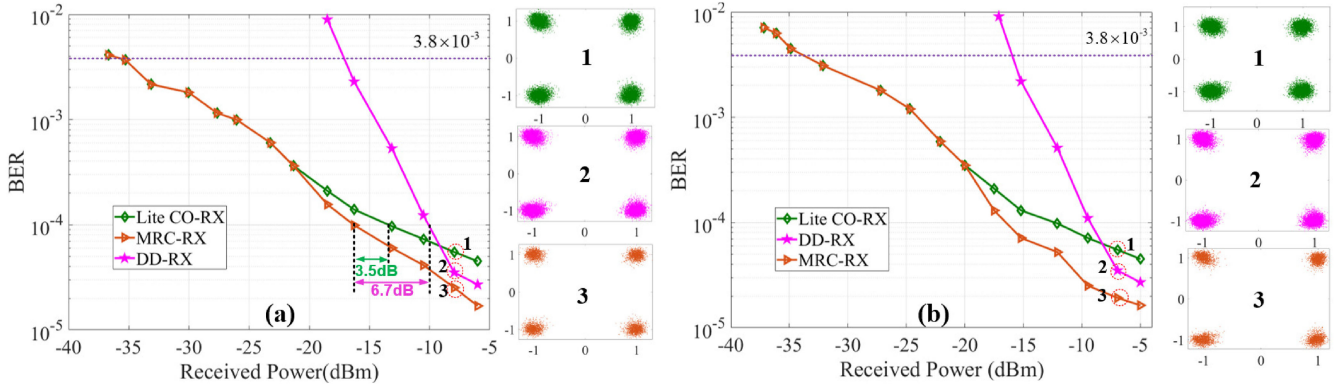


Fig. 6. Measured BERs for different receivers in the case of: (a) BTB, Insets (1)–(3): demodulated signal constellation from the lite CO-RX, DD-RX, and MRC-RX at points 1–3; (b) After 20-km SSMF fiber transmission, Insets (1)–(3): demodulated signal constellation from the lite CO-RX, DD-RX, and MRC-RX at points 1–3. BER: bit error rate, BTB: back-to-back, SSMF: standard single-mode fiber.

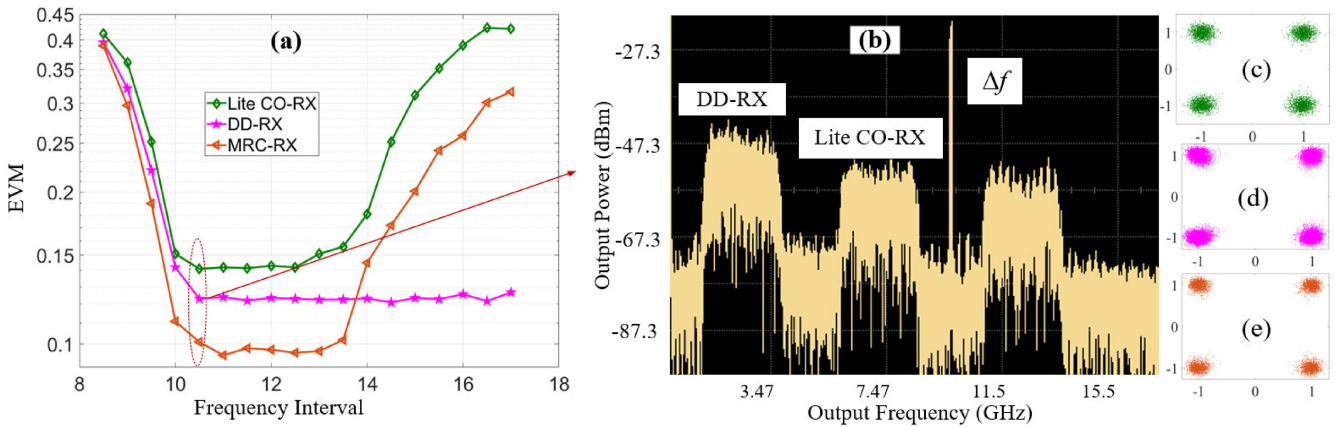


Fig. 7. (a) Measured EVM with the variation of the frequency interval between the downstream signal and upstream LO for the DD-RX, lite CO-RX, and MRC-RX after 20-km SSMF transmission; (b) Captured electrical spectra from the oscilloscope when the frequency interval was 10.5 GHz; Demodulated signal constellation from (c) lite CO-RX, (d) DD-RX, and (e) MRC-RX. EVM: error vector magnitude, LO: local oscillator.

D. Receiver Sensitivity at Varying Fiber Distances

Fig. 8(a) illustrates the receiver sensitivity of the DD-RX, lite CO-RX, and MRC-RX at a BER of the hard-decision forward error-correction (HD-FEC) threshold 3.8×10^{-3} . From the figure, we can see that at different fiber distances, the sensitivities of the lite CO-RX and MRC-RX are better, as compared to that of the DD-RX. When the fiber distance is 20 km, the lite CO-RX and MRC-RX have approximately 18.1-dB sensitivity advantage over the DD-RX. As the SNR vanishes due to the low sensitivity of direct detection, the performance of the MRC-RX is totally determined by the lite CO-RX; thus, it can achieve the same sensitivity as the lite CO-RX. The results in Fig. 6 and Fig. 8(a) indicate that, by using the MRC-RX, the system sensitivity at the HD-FEC threshold can be maintained similar to that of coherent detection. Fig. 8(b) presents the different receiver sensitivities at the BER of 1×10^{-4} . Unlike the results in Fig. 8(a), because of the contribution of the DD-RX, a higher receiver sensitivity can always be achieved for the MRC-RX than that for the lite CO-RX and DD-RX.

E. Performance Comparison for MRC-RX in Silicon Modulator System and LiNbO₃ Modulator System

To further evaluate the effectiveness of the MRC-RX and provide a comparative study, the same system using a commercially available LiNbO₃ MZM (iXblue MXAN-LN-40) was implemented. The SFDR of the LiNbO₃ MZM for SHD and IMD3 were measured using the same linearity measurement setup as depicted in Fig. 4(a). The values of $97.5 \text{ dB}\cdot\text{Hz}^{1/2}$ and $113.6 \text{ dB}\cdot\text{Hz}^{2/3}$ were achieved for SHD and IMD3, respectively, which are much better than those of the silicon modulator. Normally, a higher received optical power will yield a higher SFDR; thus, the SFDR value can be increased further by increasing the received optical power. In our measurements, we maintained the same optical power reaching the photodetector after amplification for both the Si MZM and LiNbO₃ MZM cases. The measured system BER performances are shown in Figs. 9(a)–(b) for BTB and 20-km SSMF transmission, respectively. For the measurements, the system setups were the same for Si MZM and LiNbO₃ MZM. It can be seen that, for both the

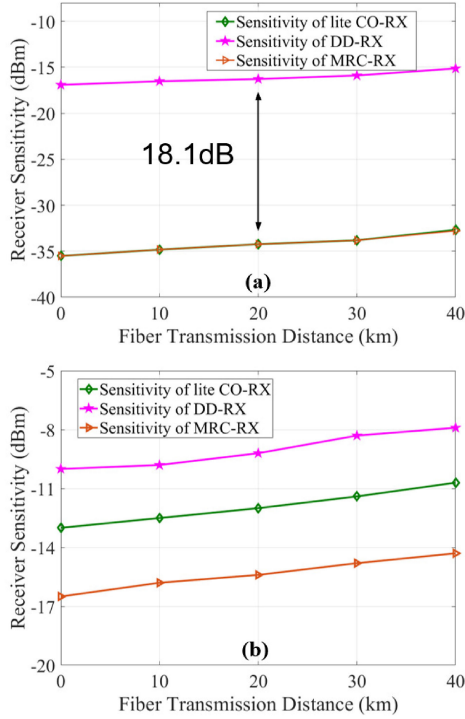


Fig. 8. Receiver sensitivity of the DD-RX, lite CO-RX, and MRC-RX at different SSMF transmission distances at BERs of: (a) HD-FEC threshold, (b) 1×10^{-4} . HD-FEC: hard-decision forward error-correction.

BTB and 20-km SSMF transmission cases, the performances of the DD-RX, lite CO-RX, and MRC-RX are all better in the case of LiNbO₃ MZM than that of Si MZM, due to the better linearity of the LiNbO₃ modulator. For this analog system, with a better modulator linearity, the distortion of the modulated optical signal will be smaller, and it will be easier for the receiver to recover the original signals. For the MRC-RX, similar to that in Fig. 6, for both the cases employing the Si MZM and LiNbO₃ MZM, when the received power is lower than the DD-RX sensitivity, the MRC-RX performance is completely determined by the lite CO-RX. When the received power becomes larger than the DD-RX sensitivity, the MRC-RX can achieve a better BER performance than those of the DD-RX and lite CO-RX separately.

However, for the MRC-RX of the Si MZM system, in both the BTB and 20-km SSMF transmission cases, when the received power is larger than the DD-RX sensitivity, a better BER performance can be achieved than those of the lite CO-RX and DD-RX in the LiNbO₃ MZM system. In the experiments, at the BER of 1.0×10^{-4} , receiver sensitivity improvements of 1.1 dB and 5.6 dB were obtained compared with the lite CO-RX and DD-RX in the LiNbO₃ MZM system, respectively, as shown in Fig. 9(a). This indicates that by using the MRC-RX, the system performance degradation caused by the low linearity of the Si MZM can be effectively reduced, compared with the case using a commercial LiNbO₃ MZM without the MRC-RX. For both the Si MZM and LiNbO₃ MZM cases, when the received power becomes larger than one threshold, the DD-RX performs better than the lite CO-RX because it is immune to the phase-related impairments generated by the beating of different lasers.

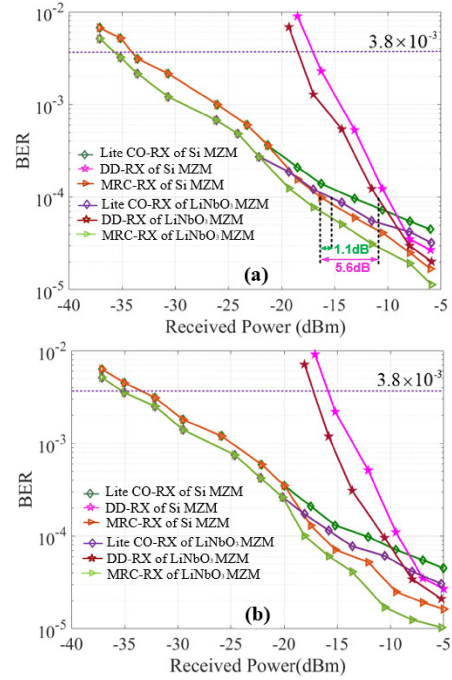


Fig. 9. Measured BER curves vs. received power for (a) BTB, and (b) 20-km SSMF transmission when using Si MZM and LiNbO₃ MZM. BTB: back to back, SSMF: standard single-mode fiber.

IV. DISCUSSION

Because of the high bandwidth of the silicon modulator (33 GHz at 4-V bias voltage), the signal modulation rate and level in the experiment can be further increased by employing a much higher bandwidth PD.

In our experiment, the receiver sensitivity of the lite CO-RX at the HD-FEC threshold, as shown in Figs. 6 and 9, is not as efficient as the state-of-art works, because the LO laser linewidth employed in the experiment was ~ 1.5 MHz. As discussed in [29], [30], the phase noise generated by the LO could pass through the equalization, which will generate equalization-enhanced phase noise. The EVM of the signal can be expressed in terms of the group velocity dispersion parameter (β_2), fiber length (L), transmitted symbols per second (Baud rate = $1/T_s$, T_s is the symbol period), and linewidth of the laser (LW): $EVM^2 \approx \pi^2 \cdot |\beta_2| \cdot L \cdot \text{Baudrate} \cdot LW$. This indicates that, when the linewidth of the LO is large, a large EVM will result, which will degrade the BER performance [31]. The sensitivity at the HD-FEC threshold in our system can be further improved (< -35 dBm) by employing a lower linewidth ($< \sim 150$ kHz) laser [29], [30].

Generally, after the square law detection of PD for the input signals, as shown in our system, the signal-to-signal beat interference (SSBI) occupies the same bandwidth as the signal from zero frequency. However, in our experiments, due to the wide guard band and high input carrier-to-signal power ratio (CSPR, ~ 12 dB), the influence of the SSBI on the system is marginal [32]–[34].

In practical system, the photonic integrated electrically controllable PC as shown in [35], [36] can be used to replace the traditional manually controlled PC by electrically controlling.

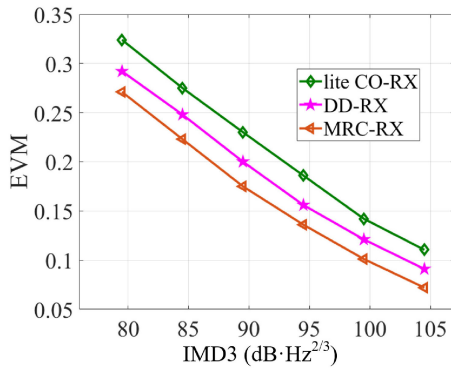


Fig. 10. Simulated EVM with the variation of the IMD3 of the modulator for DD-RX, lite CO-RX, and MRC-RX, respectively.

The system demonstrated in this work is an analog microwave optics link (the downstream QPSK signal is first generated by an AWG, and then converted to intermediate frequency analog waves to drive the Si modulator), the low linearity of the employed Si modulators will strongly affect the overall performance of the system [37]. The DD-RX and lite CO-RX components are both generated by the beating between different optical carriers and signal sidebands, with a worse modulator linearity, the SNR of the generated DD-RX and lite CO-RX components will be lower which will result in a degraded system performance [37]. To further characterize the nonlinearity compensation capability of the proposed MRC-RX, the EVM performance versus the nonlinearity of the modulator (IMD3) are simulated for DD-RX, lite CO-RX and MRC-RX, respectively [38]. The results are shown in Fig. 10. From Fig. 10 we can see that when the IMD3 value is low ($< \sim 90$ dB·Hz^{2/3}), which corresponds to a poor modulator linearity, the EVMs of the lite CO-RX, DD-RX and MRC-RX are all bad. And when the IMD3 value is large enough ($> \sim 95$ dB·Hz^{2/3}), the EVMs for all the receivers are becoming better. When the IMD3 is about 100 dB·Hz^{2/3} (similar as the measured value by experiment), the achieved EVMs for lite CO-RX, DD-RX and MRC-RX are 14.20%, 12.10%, and 10.11%, respectively, which match well with the experiment results shown in Fig. 7. The results indicate that the distortion produced by the nonlinearity of the modulator is the most significant negative impact to the performance of the system. And by employing the MRC-RX, in different cases of IMD3 value, a better EVM performance can always be achieved than lite CO-RX and DD-RX. The results prove the nonlinearity compensation capability of MRC-RX in different cases. More details about the simulation can be found in our previous work [38].

In our experiment, single-arm driving mode was employed to drive the Si modulator. Similar driving method and measured linearity results can also be found in our previous work [39].

The cost and complexity of the system are comparable with the pure lite coherent systems, such as those reported in [4], [7]. Compared to these two works, no additional equipment/device was required in this study. The only difference is the DSP after the PD. Besides the DSP for lite coherent detection, the DSP for direct detection and the MRC algorithm were added in MRC-RX. The cost and complexity of the system do not

increase significantly, except the additional DSPs. These extra DSPs could achieve a more reliable transmission through optimized receiver sensitivity and mitigate the system performance degradation induced by the silicon modulator. A higher receiver sensitivity can reduce the cost for error correction and enable a higher split ratio and longer reach, which can reduce the deploying cost for telecom operators. As the highest frequency of the generated components in the MRC-RX is the same as that with the lite CO-RX case, there are no higher requirements of the analog-to-digital (ADC) device compared with the lite CO-RX. Based on these considerations, we believe that adding the extra DSPs is reasonable. Moreover, from the system level, because of the CMOS compatibility and low-cost mass production of the silicon modulator, the cost can be further reduced by large-scale silicon modulator deployment in access.

For ONU and OLT in the near future, integrating multiple devices, such as laser, modulator, PD, passive devices, and electronic circuits, onto a chip can significantly reduce the cost and power consumption [40], [41], which will greatly benefit the operators and end users.

V. CONCLUSION

A novel MRC-RX that combines a DD-RX and lite CO-RX is proposed and has been experimentally demonstrated to mitigate the system performance degradation induced by the silicon modulator in PON based access. By employing the proposed MRC-RX, an optimized receiver sensitivity and a more reliable transmission in both cases of low and high received power were achieved. In the proof-of-concept experiment, at the BER of 1.0×10^{-4} , the MRC-RX receiver sensitivity was improved by 3.5 dB and 6.7 dB compared with the lite CO-RX and DD-RX, respectively. The frequency interval between the generated DD-RX component and lite CO-RX component should be carefully arranged to avoid frequency overlap, which may cause severe performance degradation. The optimal frequency interval in the experiment is between 10 and 14 GHz; by setting the frequency interval properly, 28.5% EVM improvement can be achieved. Comparing with a system that employs a commercial LiNbO₃ modulator, a maximum improvement of ~ 5.6 dB of the receiver sensitivity was obtained for the MRC-RX in the silicon modulator system; thus, the system performance degradation caused by the low linearity of the silicon modulator can be effectively reduced by employing the MRC-RX. The proposed MRC-RX makes sense to the building of next generation high reliable photonics integrated access by employing silicon modulators in 5G era.

REFERENCES

- [1] M. Phil, "What applications are driving higher capacity in access?" in *Proc. Opt. Fiber Commun. Conf., Opt. Soc. America*, 2018, Paper M2B.1.
- [2] M. S. Erkinç *et al.*, "Comparison of low complexity coherent receivers for UDWDM-PONs," *J. Lightw. Technol.*, vol. 36, no. 16, pp. 3453–3464, Aug. 15, 2018.
- [3] Next Generation Mobile Networks (NGMN) Alliance, "5g white papers," [Online]. Available: <https://www.ngmn.org/5g-white-paper/5g-white-paper.html>.
- [4] M. S. Erkinç *et al.*, "Bidirectional wavelength-division multiplexing transmission over installed fibre using a simplified optical coherent access transceiver," *Nature Commun.*, vol. 8, no. 1, 2017, Art. no. 1043.

- [5] Huawei Technologies Co. Ltd., "Next-generation PON evolution," 2013, [Online]. Available: www.huawei.com/ilink/en/download/HW_077443.
- [6] D. Nasset, "Ng-pon2 technology and standards," *J. Lightw. Technol.*, vol. 33, no. 5, pp. 1136–1143, Mar. 1, 2015.
- [7] Q. Zhou *et al.*, "Symmetric long-reach 16-QAM transmission using lite coherent receiver for next-generation optical access network," in *Proc. Opt. Fiber Commun. Conf., Opt. Soc. America*, 2019, Paper Th2A.29.
- [8] S. J. Savory, "Digital coherent optical access networks," in *Proc. IEEE Int'l. Photon. Conf.*, 2013, Paper MG2.1.
- [9] X. Liu, H. Zeng, N. Chand, and F. Effenberger, "Efficient mobile fronthaul via dsp-based channel aggregation," *J. Lightw. Technol.*, vol. 36, no. 6, pp. 1556–1564, Mar. 2016.
- [10] B. Bai, H. Shu, X. Wang, and W. Zou, "Towards silicon photonic neural networks for artificial intelligence," *Sci. China Inf. Sci.*, vol. 63, no. 6, 2020, Art. no. 160403.
- [11] G. T. Reed, G. Mashanovich, F. Y. Gardes, and D. J. Thomson, "Silicon optical Modulators," *Nature Photon.*, vol. 4, no. 8, pp. 518–526, 2010.
- [12] Q. Xu, B. Schmidt, S. Pradhan, and M. Lipson, "Micrometre-scale silicon electro-optic modulator," *Nature*, vol. 435, no. 7040, pp. 325–327, 2005.
- [13] M. Li, L. Wang, X. Li, X. Xiao, and S. Yu, "Silicon intensity Mach Zehnder modulator for single lane 100 Gb/s applications," *Photon. Res.*, vol. 6, no. 2, pp. 109–116, 2018.
- [14] R. Ding *et al.*, "High-speed silicon modulator with slow-wave electrodes and fully independent differential drive," *J. Lightw. Technol.*, vol. 32, no. 12, pp. 2240–2247, Jun. 15, 2014.
- [15] P. Dong *et al.*, "Monolithic silicon photonic integrated circuits for compact 100+ Gb/s coherent optical receivers and transmitters," *IEEE J. Sel. Top. Quantum Electron.*, vol. 20, no. 4, pp. 150–157, Jul./Aug. 2014.
- [16] A. Samani *et al.*, "Experimental parametric study of 128 Gb/s PAM-4 transmission system using a multi-electrode silicon photonic Mach Zehnder modulator," *Opt. Express*, vol. 25, no. 12, pp. 13252–13262, 2017.
- [17] E. Timurdogan *et al.*, "An ultralow power athermal silicon modulator," *Nature Commun.*, vol. 5, no. 1, 2014, Art. no. 4008.
- [18] P. Dong, L. Chen, and Y. K. Chen, "High-speed low-voltage single-drive push-pull silicon Mach-Zehnder modulators," *Opt. Express*, vol. 20, no. 6, pp. 6163–6169, 2012.
- [19] G. Cong and M. Ohn, "Silicon traveling-wave Mach-Zehnder modulator under distributed-bias driving," *Opt. Lett.*, vol. 43, pp. 403–406, 2018.
- [20] M. He *et al.*, "High-performance hybrid silicon and lithium niobate Mach-Zehnder modulators for 100 Gbit/s-1 and beyond," *Nature Photon.*, vol. 13, no. 5, pp. 359–364, 2019.
- [21] M. Streshinsky *et al.*, "Highly linear silicon travelling wave Mach-Zehnder carrier depletion modulator based on differential drive," *Opt. Express*, vol. 21, no. 3, pp. 3818–3825, 2013.
- [22] J. Ding, S. Shao, L. Zhang, X. Fu, and L. Yang, "Method to improve the linearity of the silicon Mach-Zehnder optical modulator by doping control," *Opt. Express*, vol. 24, no. 21, pp. 24641–24648, 2013.
- [23] L. Kahn, "Ratio Squarer," in *Proc. IRE*, 1954, Art. no. 1704.
- [24] C. Guo, J. Liang, and R. Li, "Long-reach SSB-OFDM-PON employing fractional sampling and super-Nyquist image induced aliasing," *J. Opt. Commun. Netw.* vol. 7, no. 12, pp. 1120–1125, 2015.
- [25] C. Tepedelenlioglu and R. Challagulla, "Low-complexity multipath diversity through fractional sampling in OFDM," *IEEE Trans. Signal Process.*, vol. 52, no. 11, pp. 3104–3116, Nov. 2004.
- [26] M. Oerder and H. Meyr, "Digital filter and square timing recovery," *IEEE Trans. Commun.*, vol. 36, no. 5, pp. 605–612, May 1988.
- [27] M. Morelli and U. Mengali, "Feedforward frequency estimation for PSK: A tutorial review," *Eur. Trans. Telecommun.*, vol. 9, no. 2, pp. 103–116, 1998.
- [28] Z. Tao *et al.*, "Improvements to digital carrier phase recovery algorithm for high-performance optical coherent receivers," *IEEE J. Sel. Topics Quantum Electron.*, vol. 16, no. 5, pp. 1201–1209, Sep./Oct. 2010.
- [29] G. Jacobsen *et al.*, "Influence of pre- and post-compensation of chromatic dispersion on equalization enhanced phase noise in coherent multilevel systems," *J. Opt. Commun.*, vol. 32, no. 4, pp. 257–261, 2012.
- [30] A. Kakkar *et al.*, "Comprehensive study of equalization-enhanced phase noise in coherent optical systems," *J. Lightw. Technol.*, vol. 33, no. 23, pp. 4834–4841, Dec. 1, 2015.
- [31] B. Nebendahl *et al.*, "Quality metrics in optical modulation analysis: EVM and its relation to Q-factor, OSNR, and BER," in *Proc. Asia Commun. Photon. Conf. OSA Tech. Dig. (online) Opt. Soc. America*, 2012, Paper AF3G.2.
- [32] S. Le *et al.*, "1.72tb/s virtual-carrier-assisted direct-detection transmission over 200km," *J. Lightw. Technol.*, vol. 36, no. 6, pp. 1347–1353, Mar. 15, 2018.
- [33] W. Shieh, C. Sun, and H. Ji, "Carrier-assisted differential detection," *Light. Sci. Appl.*, vol. 9, no. 18, pp. 1–9, 2020.
- [34] Y. Zhu, L. Li, Y. Fu, and W. Hu, "Symmetric carrier assisted differential detection receiver with low complexity signal-signal beating interference mitigation," *Opt. Express*, vol. 28, no. 13, pp. 19008–19022, 2020.
- [35] C. Doerr and L. Chen, "Monolithic PDM-DQPSK receiver in silicon," in *Proc. of Eur. Conf. Exhib. Opt. Commun.*, 2010.
- [36] W. D. Sacher, T. Barwicz, B. J. F. Taylor, and J. K. S. Poon, "Polarization rotator-splitters in standard active silicon photonics platforms," *Opt. Express*, vol. 22, no. 4, pp. 3777–3786, 2014.
- [37] B. Dingel, N. Madamopoulos, and A. Prescod, "Chapter 5: adaptive high linearity intensity modulator for advanced microwave photonic links," in *Proc. Book of Opt. Commun. Technol.*, 2017.
- [38] Y. Tao *et al.*, "Numerical investigation of the linearity of graphene-based silicon waveguide modulator," *Opt. Express*, vol. 27, no. 6, pp. 9013–9031, 2019.
- [39] T. Li *et al.*, "Demonstration of 6.25 Gbaud advanced modulation formats with subcarrier multiplexed technique on silicon Mach-Zehnder modulator," *Opt. Express*, vol. 22, no. 16, pp. 19818–19823, 2014.
- [40] Y. Shen *et al.*, "Silicon photonics for extreme scale systems," *J. Lightw. Technol.*, vol. 37, no. 2, pp. 245–260, Jan. 2019.
- [41] M. Rakowski *et al.*, "45nm CMOS - Silicon Photonics Monolithic Technology (45CLO) for next-generation, low power and high speed optical interconnects," in *Proc. Opt. Fiber Commun. Conf., Opt. Soc. America*, 2020, Paper T3H.3.

Jun Qin received the Ph.D. degree from the State Key Laboratory of Information Photonics and Optical Communications, School of Information and Telecommunication Engineering, Beijing University of Posts and Telecommunications, Beijing, China, in 2016, for work on an optical information and communication system. From 2016 to 2018, he worked with Huawei Beijing Research Center as a Standard Engineer, focused on the standardization work of optical network in IETF. He is currently a Postdoctoral Fellow with the State Key Laboratory of Advanced Optical Communication Systems and Networks, Department of Electronics, School of Electronics Engineering and Computer Science, Peking University, Beijing. His research interests include silicon photonics, nonlinear effect-based all-optical signal processing in a silicon platform, and integrated communication systems.

Yuansheng Tao received the B.S. degree from the School of Optoelectronic Science and Engineering, University of Electronic Science and Technology of China, Chengdu, China, in 2017. He is currently working toward the Ph.D. degree with the School of Electronic Engineering and Computer Science, State Key Laboratory of Advanced Optical Communication Systems and Networks, Peking University, Beijing, China. His current research interests include silicon-based integrated microwave photonics.

Haowen Shu received the Ph.D. degree from the Peking University, Beijing, China, in 2020. He is currently a Postdoctoral Fellow with the State Key Laboratory of Advanced Optical Communication Systems and Networks, Department of Electronics, School of Electronics Engineering and Computer Science, Peking University. His research interests are in photonics integrated circuits and on-chip telecommunication systems.

Siming Liu received the Ph.D. degree from the State Key Laboratory of Information Photonics and Optical Communications, School of Information and Telecommunication Engineering, Beijing University of Posts and Telecommunications, Beijing, China, in 2018, for work on radio over fiber system. Since 2018, he has been with Huawei Beijing Research Center, Beijing, as an Algorithm Engineer in digital signal processing.

Danshi Wang received the Ph.D. degree in electromagnetic field and microwave technology, in 2016, from the Beijing University of Posts and Telecommunications, Beijing, China, where he is currently a Lecturer with the Institute of Information Photonics and Optical Communications. His research interests include optical transmission and optical signal processing, artificial intelligence, machine learning, and wavelength switched optical networks.

Rahul Kumar Gangwar received the Ph.D. degree from the Indian Institute of Technology (Indian School of Mines), Dhanbad, India, in 2017. From 2017 to 2018, he was a Postdoctoral Fellow with the Center for Applied Photonics, INESC TEC, Porto, Portugal. Since 2019, he has been a Postdoctoral Fellow with the School of electronic engineering and computer science, Peking University, Beijing, China. His current research interests include integrated optical sensors and plasmonic sensors.

Guo-Wei Lu (Member, IEEE) received the Ph.D. degree in information engineering from The Chinese University of Hong Kong (CUHK), Hong Kong, in 2005. From 2005 to 2006, he was a Postdoctoral Fellow with CUHK. From 2006 to 2009, he was an Expert Researcher with the National Institute of Information and Communications Technology (NICT), Tokyo, Japan. From 2009 to 2010, he was an Assistant Professor with the Chalmers University of Technology, Göteborg, Sweden. From 2010 to 2014, he was a Researcher with NICT. During 2014–2020, he was with Tokai University as an Associate Professor. Since 2020, he joined the University of Aizu as a Senior Associate Professor. He is currently a Visiting Researcher with NICT since 2014, and a Visiting Lecturer with Kyushu University, Fukuoka, Japan, since 2018. His current research interests include advanced optical modulation formats, electro-optic modulators, photonic signal processing, and optical parametric amplifiers.

Xingjun Wang received the B.E., M.E., and Ph.D. degrees from the Dalian University of Technology, Dalian, China, in 1999, 2002, and 2005, respectively. From 2007 to 2009, he was a JSPS Postdoctoral Fellow with the Department of Electronic Engineering, University of Electro-Communications, Chofu, Japan. In 2009, he joined Peking University, Beijing, China, and is currently a Full Professor with Peking University. In 2015, he was selected first Young Yangtze River Scholar of China. Now he is devoted into the research and development of large-scale integrated chips and systems based on photonic and electronic devices and systems. He is interested in optical transceiver chips and systems for data centers, microwave photonic chips and systems, silicon-based optical amplifiers and lasers, silicon-based sensors/nonlinear and the application of 2-D material on silicon-based devices.